THE JOURNAL OF PHYSICAL CHEMISTRY C
A JOURNAL OF THE AMERICAN CHEMICAL SOCIETY

pubs.acs.org/JPCC
Article

Investigating Variable Irradiation Damage Response in Monazite, $La_{1-x}Ln_xPO_4$ (*Ln* = Pr, Nd, and Sm) Solid Solution Ceramics

Mara McCleary, Andrey Bukaemskiy, Martina Klinkenberg, Celina Erven, Sara E. Gilson, Daniil Shirokiy, Jenna Poonoosamy, Felix Brandt, Christoph Hennig, Andrew Fitch, Shavkat Akhmadaliev, Nina Huittinen, and Gabriel L. Murphy*

Cite This: *J. Phys. Chem. C* 2026, 130, 11847−11858

Read Online

ACCESS | Metrics & More | Article Recommendations | Supporting Information

ABSTRACT: Monazite ($LnPO_4$) materials are promising waste forms for immobilizing minor actinides, but their radiation damage performance as mixed solid solutions remains poorly described. Herein, we have systemically examined the irradiation response of mixed monazite solid solutions, $(La_{1-x}Ln_x)PO_4$ (x = 0, 0.5, and 1; *Ln* = Pr, Nd, and Sm), using 14 MeV $^{197}Au^{4+}$ ion irradiations at a fluence of 1×10^{15} ions/cm^2 regarding structural, microstructural, and mechanical properties. Amorphization susceptibility was assessed by grazing incidence X-ray diffraction, with the optimal incidence angle determined from stopping and range of ions in matter simulations and X-ray penetration depth calculations. Complementary characterization via scanning electron microscopy, Raman spectroscopy, and Vickers indentation provided insight into microstructural evolution, local chemistry, and mechanical property changes, respectively. The results indicate an increasing radiation damage resistance of end-member $LnPO_4$ materials with decreasing *Ln* cation size. In mixed solid solutions, $(La_{0.5}Ln_{05})PO_4$, the radiation damage resistance decreases as the size mismatch between the *Ln* cations increases, which is attributed to nonideal solid solution cation mixing during irradiation damage. We propose that irradiation-induced lattice displacements increasingly impede cation redistribution and promote structural disorder as the cation size mismatch increases, with measurable consequences for both chemical stability and mechanical integrity. The role of grain boundaries and the susceptibility to changes in local coordination chemistry of cations are further highlighted as determinants for specific irradiation damage response and their ability to act as sinks for ion and defect migration. The investigation underscores the need to evaluate complex solid solutions rather than idealized end-member compositions when assessing ceramic nuclear waste form performance for radionuclide immobilization.

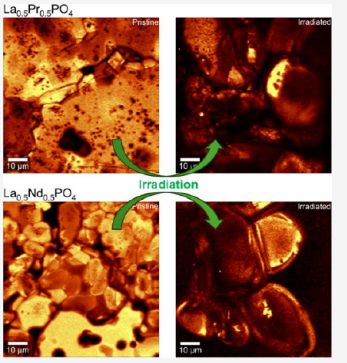

INTRODUCTION

The progressive transition toward carbon neutrality has reinvigorated interest in nuclear energy toward providing stable base load power while maintaining energy security and fuel sovereignty. Invariably, challenges remain regarding the disposal of spent nuclear fuel (SNF) that is expected to amplify with increasing uptake of power reactor units. As opposed to direct disposal of SNF, an alternative approach pursued and considered by some nations is partitioning and subsequent ceramic waste form immobilization.[1] This method enables the most challenging radionuclides, such as the trivalent minor actinides (MAs) consisting of Am and Cm, to be consolidated and immobilized, reducing waste amounts while providing enhanced safeguarding against inadvertent environmental release or nefarious use. Of ceramic waste forms considered, monazite, $LnPO_4$ (*Ln* = La, Pr, Nd, Sm), has attracted significant attention, owing to its resistance to radiation-induced metamictization.[2−4] Subsequently, this in turn has garnered focus toward potential applications for MA immobilization in addition to providing a well-defined model system for exploring radiation damage effects in solids.

A plethora of studies are present in the literature on monazite materials, primarily focused on end-member compositions.[2,5] In the case of mixed solid solutions, $(Ln'_{1-x}Ln''_x)PO_4$, there is considerably less information available, particularly regarding radiation damage response. For the immobilization of MAs within a waste form matrix, it is generally accepted that a solid solution will be formed with MAs within a larger solid matrix,[6] often containing solutes that can inhibit radiation damage cascade effects or control criticality.[7] For example, using a neutron absorber such as Gd yields $Am_{1-x}Gd_xPO_4$ as a solid solution to control criticality. Thus, the structural versatility of mixed solid solution monazites may provide a customizable immobilization matrix that can be tailored to the MAs. At the same time, it is known that solid solutions generally exhibit different chemical,

Received: June 10, 2026
Revised: July 20, 2026
Accepted: July 21, 2026
Published: August 5, 2026

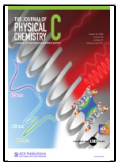

https://doi.org/10.1021/acs.jpcc.6c03822
J. Phys. Chem. C 2026, 130, 11847−11858

radiation damage response, and thermodynamic behavior to end-member materials owing to subtle differences in structure and enthalpic mixing.[8] For instance, it was recently shown in the case of $(La_{1-x}Ce_x)PO_4$ for x = 0, 0.25, 0.5, 0.75, and 1 when subject to 14 MeV $^{197}Au^{4+}$ ions with fluences of 1×10^{14} and 1×10^{15} ions/cm^2 loss of crystal and microstructural integrity was most pronounced with the solid solution compositions, particularly those possessing uneven distributions of cations (x = 0.25 and x = 0.75).[3] The reduced radiation response was attributed to poor restructuring of the cations during the irradiation and subsequent recovery process. This variable difference in structural and chemical performance against radiation damage depending upon solid solution mixing invites the open question: How does the radiation damage response performance of monazite solid solutions vary as different *Ln* cations are used? Such an endeavor provides greater insight into the behavior of MAs when potentially immobilized within ceramic monazite-based waste forms as solid solutions. Additionally, it allows the fundamental behavior of radiation damage effects to be systematically probed[2,4,9] while also allowing the performance of relevant crystalline waste form materials to be examined, regarding variable bulk performance over long time scales against radiation damage.

In order to examine the variable response to radiation damage of solid solution monazite materials, the present investigation has examined solid solutions of $(La_{1-x}Ln_x)PO_4$ with *Ln* = Pr, Nd, and Sm, for x = 0, 0.5, and 1, under 14 MeV $^{197}Au^{4+}$ ion irradiation at a fluence of 1×10^{15} ions/cm^2. Variable changes to the microstructure were examined by using scanning electron microscopy (SEM). Stopping and range of ions in matter (SRIM) calculations were performed to probe the depth of damage penetration and subsequently inform grazing incidence synchrotron X-ray diffraction (GI-XRD) measurements, which allowed the degree of relative amorphization to be probed in radiation-damaged regions of the samples. Changes to the local chemical structure and coordination chemistry of the materials were further probed via Raman microscopy through surface-mapping measurements. Finally, mechanical measurements via Vickers indentation measurements were performed to assess changes to integrity from radiation damage against the monazite solid solution chemistry. The results of the investigation are discussed regarding the pertinence of considering mixed solid solutions over end-member ceramics as nuclear waste form materials for MA immobilization regarding probing stability and integrity against radiation-induced degradation.

EXPERIMENTAL SECTION

Synthesis and Characterization

Rhabdophane powders ($LnPO_4 \times 0.67H_2O$) were prepared via a previously described precipitation method[2] and used as precursors for monazite synthesis and ceramic preparation, as also previously achieved.[3] Targeted stoichiometric additions of lanthanum, praseodymium, neodymium, and samarium nitrates (99.99%, Sigma-Aldrich) were dissolved in deionized water. Precipitation of rhabdophane was induced by the addition of phosphoric acid (85%, Sigma-Aldrich). The precipitates were separated and washed several times using deionized water with subsequent separation via centrifugation. For the final wash step, the solid was separated and suspended in 0.1 M HNO_3 and left to sit overnight. The acid was then decanted off and the solid calcined for 3 h at 120 °C in air, prior to further calcination at 500 °C in air for 2 h to generate the monazite. The calcined products were ground to a fine powder by using an agate mortar and pestle before compacted as green pellets using an Oehlglass, Hahn and Kolb MP12 uniaxial cold press by applying a force of 38 kN (p = 450 MPa). Pellets were then sintered in a tube furnace in air at 1400 °C for 5 h. Densities of the sintered ceramics were calculated through geometric and hydrostatic weighing as dictated by Archimedean and modified Archimedean methods.[10] The ceramic pellets were polished using abrasive silicon carbide paper and 1 μm diamond paste on an automatic polishing table for approximately 15 min.

Ion Irradiations

Sintered and polished ceramic pellet samples were mounted on Si wafers and one-half of the pellets was covered with Al foil to protect it from irradiation. The implantation chamber was evacuated to approximately 3×10^{-7} mbar and the samples with the sample-holder were cooled to 77 K with liquid nitrogen to reduce the thermal load at the sample surface during irradiation. All samples were irradiated with 14 MeV $^{197}Au^{4+}$ ions using a current density of 25−30 nA/cm^2 to achieve fluences of 1×10^{15} ions/cm^2. The irradiations were performed at the Ion Beam Center at the Helmholtz-Zentrum Dresden-Rossendorf (HZDR), Germany, using the 3 MV Tandetron ion accelerator. The penetration depth of the Au ions into the monazite ceramics was calculated to be approximately 2 μm for all samples using the Stopping and Range of Ions in Matter (SRIM) Monte Carlo simulation code,[11] details are provided in Supporting Information Note 1.

Scanning Electron Microscopy

Irradiated and pristine pellet samples were analyzed with an Apreo (Thermo Scientific, Netherlands) SEM using a high voltage of 1 kV and varying beam current, depending on the charging of the sample, and a working distance of 4 mm. Both irradiated and pristine regions of irradiated samples were characterized with SEM.

Raman Spectroscopy

Raman measurements were performed using a Witec alpha300 Ri inverted confocal Raman microscope with a Nikon CF plan 100× objective of numerical aperture 0.95. The instrument used an Nd:YAG laser (λ = 532 nm), a thermoelectrically cooled (CCD) Camera, and an Ultra-High-Throughput Spectrometer UHTS300. 80 × 80 μm Raman maps and spectra were generated in the wavenumber range of 300−3500 cm^{-1}. Measurements were taken at room temperature with an integration time of 0.2 s, a step size of 1 μm, using a cover glass and a grating of 1800 grooves/mm. For the final presented Raman maps, the data were normalized to the strong Raman peak of the monazite structure, ν_1, corresponding to the symmetric stretching vibration of the isolated PO_4 tetrahedra, in order to gauge relative spatial changes to the local structure of the materials.

Grazing Incidence X-ray Powder Diffraction

To investigate and monitor the relative amorphization arising from ion irradiation, the irradiated pellets were investigated using synchrotron GI-XRD at the beamline ID24 of the ESRF,[12] Grenoble, France. The data were collected using a highly collimated, monochromatic beam coupled with a 13-channel silicon 111 multianalyzer stage positioned between the sample and a Dectris Eiger2 × 2M-W cadmium telluride (CdTe) pixel detector. A specially developed goniometer was

https://doi.org/10.1021/acs.jpcc.6c03822
J. Phys. Chem. C 2026, 130, 11847−11858

used for the grazing incidence measurements.[13] An initial X-ray energy of 11.5 keV was chosen where calibration via a LaB_6 pellet standard reference yielded a precise wavelength of 1.0785 Å. The wavelength was chosen to ensure that only the surface-irradiated regions of the samples were probed by the X-rays and not the subsurface of the nonirradiated bulk. The approximate penetration depth of the X-rays was determined using the Glancing Incidence X-ray Analysis (GIXA) utility.[14] The penetration depth is defined as the distance traveled by the X-ray beam before its intensity is reduced to 1/e. Accordingly, three penetration depths cover approximately 95% of the X-ray beam attenuation. Thus, the grazing angles were selected based on the depth of radiation damage by ions that had been determined from SRIM calculations. From these calculations and ensuring that only the radiation-damaged regions were probed, an incidence grazing angle of 1° was used. Details of the depth of penetration calculations are provided in Supporting Information Note 2. Semiquantitative data analysis was performed to understand the relative amount of amorphization that had occurred in the samples. For this, peak integration was performed in the Origin software, where a consistent background with a linear baseline was applied to the samples and amorphous humps were integrated consistently.

Mechanical Testing

To determine the bulk mechanical changes to the monazite pellets from irradiation damage, specifically the microhardness and fracture toughness, Vickers indentation loading mechanical testing was performed. The microhardness (H_V) and fracture toughness (K_{1C}) were determined for both pristine and irradiated areas of the monazite pellets using a diamond Vickers indenter and subsequent analysis of the indent and crack lengths via an optical microscope. A pressure of 200 N was applied for each sample using an Anton Paar MHT-10, with a slope of 10 N/s, and a holding time of 10 s at the target pressure. The microhardness is calculated based on the size of the indentation, d, and the pressure applied, P, using eq 1.

$$H_V = \frac{0.1891 \times P}{d^2} \tag{1}$$

When fracturing, the monazite pellets in both irradiated and pristine regions were observed to produce Palmqvist cracks, as opposed to half-penny cracks; accordingly, the fracture toughness can be calculated via the Niihara equation (eq 2), where c is the fracture length as measured from the center of the indentation, E is Young's modulus, and H_V and d are defined previously.

$$K_{1C} = 0.018 H_v \sqrt{0.5d} \left(\frac{E}{H_V}\right) 0.4 \left(\frac{C}{0.5d} - 1\right)^{-1.5} \tag{2}$$

RESULTS

Microstructural Analysis

SRIM calculations, detailed in Supporting Information Note 1, found the penetration depth, based on the determined densities of sintered pellets, which are provided in Table 1, to be ~2 μm. Accordingly, all subsequent measurements were performed with this limited surface region in mind. SEM micrographs were taken on all samples on both the pristine and the irradiated sides. Figure 1 provides SEM micrographs of the pristine and irradiated end-member compositions ($LnPO_4$, Ln = La (a, b), Pr (c,d), Nd (e, f), and Sm (g, h)). From the Figure, it is apparent that all samples are affected by the irradiation, but the lighter Ln-bearing monazites, such La and Pr, present differently than the heavier ones, Nd and Pr. The light Ln's, particularly La and Pr, show a swelling of the material from irradiation, which leads to a reduction of porosity and a sealing of small cracks. After irradiation, grain boundaries can be distinguished for these two samples, which now consist of swollen, round-shaped grains. The irradiation of the Sm- and Nd-doped samples leads to a "tortellini"-like microstructure at the respective pellet's surface, i.e., the original microstructure is destroyed. In particular, the irradiated $NdPO_4$ is characterized by a completely puffed and swollen surface. The $SmPO_4$ grains are not completely puffed but show a much higher degree of swelling compared with the Pr- and La-monazites. The observed changes in the microstructure are consistent with radiation-damage-induced restructuring.

Table 1. Densities of Pristine Sintered Pellets Determined from Archimedes Measurements Where ρ_S and ρth Correspond to Sintered and Theoretical Density

composition	theoretical density (g/cm^3)	average sintered density (ρ_S/ρth %)	calculated density (g/cm^3)
$LaPO_4$	5.060	98.99(18)	5.009
$PrPO_4$	5.307	95.49(18)	5.068
$NdPO_4$	5.453	96.40(18)	5.257
$SmPO_4$	5.641	95.92(70)	5.420
$La_{0.5}Pr_{0.5}PO_4$	5.194	92.93(51)	4.794
$La_{0.5}Nd_{0.5}PO_4$	5.267	94.60(78)	4.983
$La_{0.5}Sm_{0.5}PO_4$	5.366	96.20(98)	5.162

Figure 2 provides the SEM micrograph measurements of the pristine and irradiated solid solution compositions ($La_{0.5}Ln_{0.5}PO_4$, Ln = Pr, Nd, and Sm). Similar to Figure 1, a swelling of the grain structure can be again observed in the $La_{0.5}Pr_{0.5}PO_4$ composition from irradiation, with a similar microstructure after irradiation as seen for both end members of this solid solution series (Figure 1b,d). As the heavier Ln cations are introduced, more significant transformation of surfaces can be observed, particularly pronounced in the $La_{0.5}Sm_{0.5}PO_4$ composition, very similar to the $SmPO_4$ composition seen in Figure 1. Such exfoliation in the $La_{0.5}Nd_{0.5}PO_4$-irradiated sample is also observed, far greater than that observed in the end-member compositions of $LaPO_4$ and $NdPO_4$. In comparison, the grain structure in the irradiated $La_{0.5}Sm_{0.5}PO_4$ composition, i.e., possessing a heavier Ln constituent, is barely present. Such behavior is consistent with amorphization and microstructural transformation that appears to be most pronounced with heavier Ln-bearing solid solution compositions.

Raman Spectroscopy

To further understand potential chemical changes that could have arisen variably between end-member and solid-solution-irradiated monazite materials, Raman spectroscopy mappings were performed on the $PrPO_4$ and $NdPO_4$ samples with corresponding solid solutions. Figures 3 and 4 provide, respectively, pristine and irradiated Raman maps normalized to the ν_1 PO_4 stretching mode for end members, $PrPO_4$ and $NdPO_4$, and solid solution counterparts, $La_{0.5}Pr_{0.5}PO_4$ and $La_{0.5}Nd_{0.5}PO_4$, respectively.

When the pristine Raman map areas of Figures 3 and 4 are examined, similar trends are apparent, with a particularly strong signal arising from grain regions, whereas grain

https://doi.org/10.1021/acs.jpcc.6c03822
J. Phys. Chem. C 2026, 130, 11847−11858

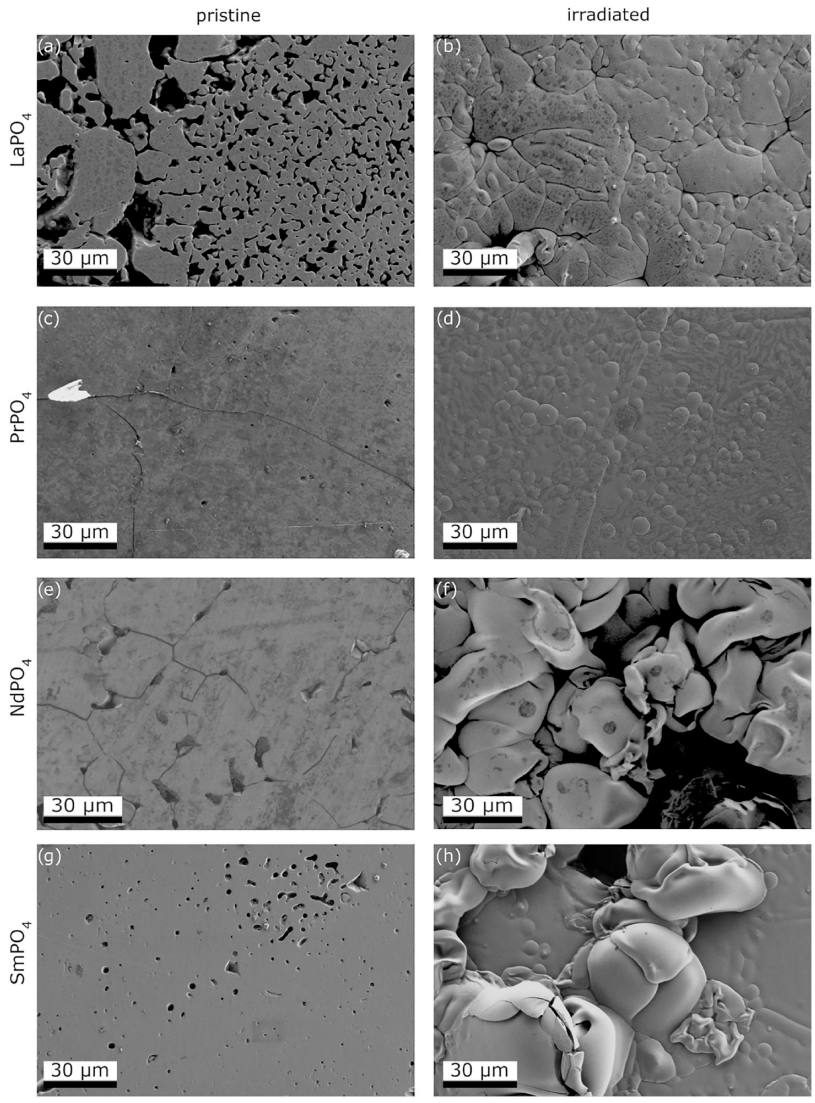

Figure 1. SEM micrographs of pristine and irradiated end-member $LnPO_4$ compositions for *Ln* = La (a, b), Pr (c, d), Nd (e, f), and Sm (g, h). Ion irradiation conditions used were 14 MeV $^{197}Au^{4+}$ with a fluence of 1×10^{15} ions/cm.

boundaries show lower intensity. Such behavior has been observed previously for the grain boundaries, where it is associated with poor crystallinity within these regions.[2] To further illustrate this effect, Figures 3 and 4 also plot the 1D Raman spectra of pristine and irradiated $NdPO_4$ based on spot measurements. Inspecting the trends of the pristine 1D spectra shows the presence of sharp peaks in addition to the subtle presence of modes at higher wavenumbers, which are discussed below. Some slight differences in Raman peak positions are seen between the pristine samples, which is related to different cations and solid solution mixing between the end-member and solid solution samples.

When the irradiated Raman maps of Figures 3 and 4 are examined, a significant loss in intensity of the main ν_1 is observed. Some residual intensity is present, but this appears to be confined to the grains, whereas grain boundaries show significant loss of intensity, far more so than observed in the pristine. Grain boundaries are known often as radiation sinks for radiation damage and this appears to follow in these Raman maps.[2,15] When the 1D Raman maps of Figure 3 and 4 are considered, further comparative loss of intensity can be observed between main Raman bands and those of the pristine samples. Again, this is more pronounced when the spot measurements of the grain boundaries are considered. It has been previously described by Ruschel that changes to the FWHM and associated broadening of Raman peaks are suitable parameters for gauging radiation damage in monazite materials.[16] Inspecting associated main peaks of the 1D Raman maps of Figures 3 and 4, there is noticeable broadening of the irradiated spectrum peaks indicative of the described irradiation damage and changes to local coordination across all Raman modes. Notably, no major shifting of Raman peaks between pristine and irradiated samples could be observed. Such changes would be indicative of local changes to the degree of cation mixing and chemistry between sample constituent ions, since the Raman position of modes for monazite is dependent on specific cation presence. This suggests that locally radiation damage is associated with the cationic coordination environment to anionic groups. Specifically, the phosphate groups, their displacement, interactions, and their ability to recombine with other cationic groups. Nevertheless, this still appears to be a cation-dependent process, as when comparing particularly irradiated grain

https://doi.org/10.1021/acs.jpcc.6c03822
J. Phys. Chem. C 2026, 130, 11847−11858

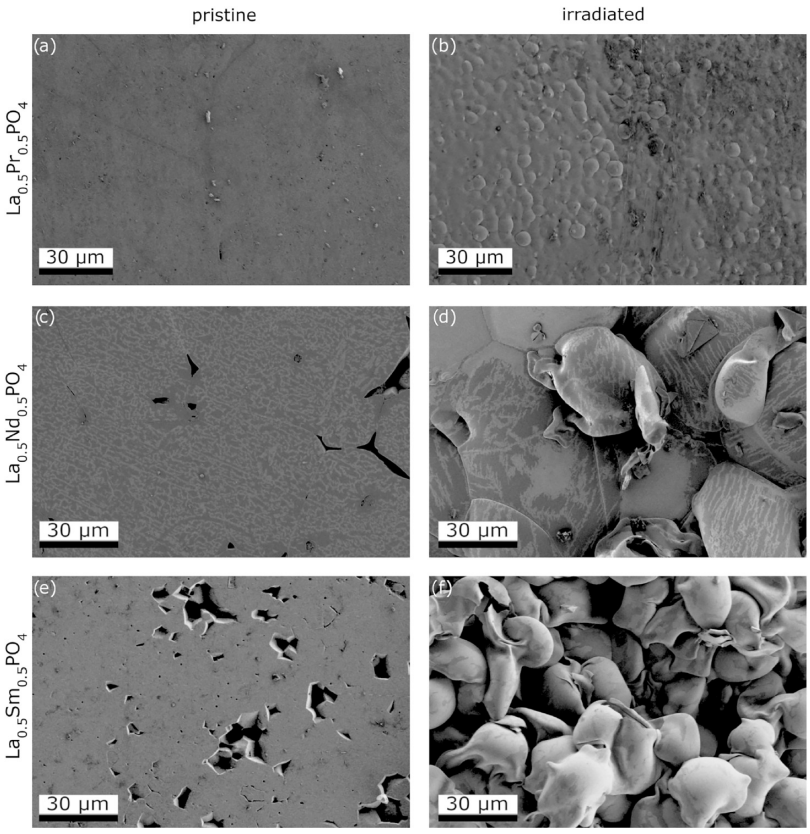

Figure 2. SEM micrographs of pristine and irradiated end-member $La_{0.5}Ln_{0.5}PO_4$ compositions for *Ln* = Pr (a,b), Nd (c,d), and Sm (e,f). Ion irradiation conditions used were 14 MeV $^{197}Au^{4+}$ with a fluence of 1×10^{15} ions/cm^2.

boundaries between end members and solid solutions, the latter has considerably more observed damage.

To further evaluate changes to the examined monazite samples from irradiation damage via Raman analysis, peak fitting was performed using the Origin software. For this analysis, pseudo-Voigt functions were applied to account for the distortion of peaks following irradiation and a least-squares minimization fitting approach was used. The analysis focused on the main ν_1 PO_4 stretching mode and changes to its full width half-maximum (FWHM), where Table 2 provides the fitted results. When the change, **Δ**, to FWHM is considered following irradiation, this is most pronounced in the grain boundary regions, where it significantly increases, indicating strong distortion occurring. Much less considerable change to the FWHM has occurred in the actual grains from the analysis, strongly indicating that the grain boundaries endure the most loss of order and distortion following irradiation.

A further significant observation from Figures 3 and 4 is the presence of pronounced signals at higher wavenumbers, above 1500 cm^{-1}, that are particularly evident for the $NdPO_4$ and also susceptibly seen for the $La_{0.5}Nd_{0.5}PO_4$ samples. Such signals cannot be attributed to vibrational modes of the PO_4 tetrahedra in monazite. To further analyze these bands, the Raman shift axis was converted to wavelengths, using eq (3)

$$\lambda(\mathrm{nm}) = \frac{10^7 \frac{\mathrm{nm}}{\mathrm{cm}}}{(18,797 - \Delta\tilde{\nu})\frac{1}{\mathrm{cm}}} \tag{3}$$

where 18,797 cm^{-1} corresponds to the excitation wavenumber of the Raman laser (532 nm) and $\Delta\tilde{\nu}$ is the measured Raman shift in cm^{-1}. The resulting spectra are presented in Figure 5 for pristine and irradiated grains and grain boundaries in $NdPO_4$. The observed bands in the 575−600 nm range coincide with the known Nd^{3+} f−f transition energies, specifically transitions from the $^4I_{9/2}$ ground state to the $^4G_{5/2}$ and $^2G_{7/2}$ excited states.[17] These signals can thereby be assigned to resonance-enhanced electronic Raman scattering rather than vibrational Raman modes. In this process, the incident 532 nm excitation is inelastically scattered with an energy loss matching the Nd^{3+} electronic transitions, resulting in scattered photons at longer wavelengths. Hence, these vibrations are observed in the $NdPO_4$ and $La_{0.5}Nd_{0.5}PO_4$ spectra of Figures 3 and 4.

It is clear from Figure 5 that irradiation damage has caused significant structural distortions in the Nd^{3+} coordination environment in $NdPO_4$, leading to a loss of the spectral fine structure. The grain boundary regions exhibit the most pronounced damage and structural degradation compared with the grain interiors. This is consistent with previous Raman observations concerning both damage appearing to be associated with changes to the coordination environment of cation centers and also the grain boundaries acting as damage sinks. Similar radiation-induced spectral broadening has been reported for Nd^{3+}-doped monazites using photoluminescence mapping in the Nd^{3+} emission range (850−950 nm).[18] In that study, a fully amorphized Nd^{3+}-doped sample was used as a reference to quantify the degree of amorphization as a function of irradiation fluence. Here, the complete loss of spectral features following irradiation in the grain boundary regions indicates a fully amorphized Nd^{3+} environment, lacking long-range order. In contrast, the grains retain some spectral fine

https://doi.org/10.1021/acs.jpcc.6c03822
J. Phys. Chem. C 2026, 130, 11847−11858

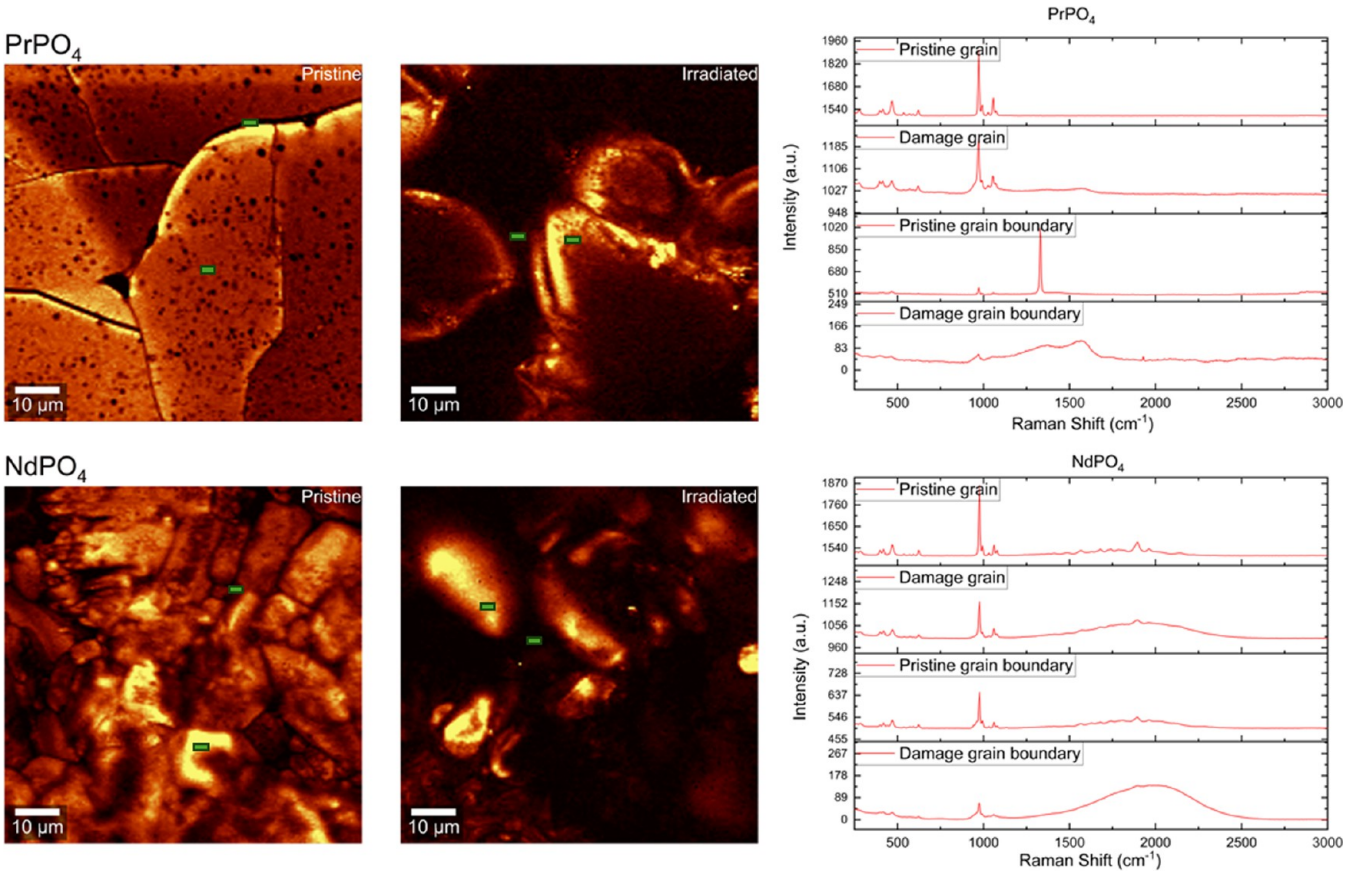

Figure 3. (Left) Raman maps of the relative intensity of the ν_1 PO_4 stretching mode for the end members $PrPO_4$ and $NdPO_4$, pristine and irradiated areas. (Right) 1D Raman spectra taken by spot measurements according to the green markers given on the Raman maps.

structure, suggesting only partial amorphization, which is in agreement with the GI-XRD data discussed below.

Grazing Incidence X-ray Diffraction

Synchrotron GI-XRD measurements were performed in order to qualitatively determine the relative degree of amorphization occurring between end-member and solution compositions. Due to the small size of the X-ray beam used (~50 μm) coupled with the relatively large average grain size maintained in irradiated regions, single-crystal diffraction peaks were frequently encountered, as has been observed previously for irradiated monazites using similar measurements.[3,19] Consequently, despite rotating samples during measurements, it was not possible to analyze the crystalline portion of the samples quantitatively from GI-XRD. In order to ensure only the surface-irradiated regions of all samples were probed from GI-XRD, a grazing angle of 1° was used consistently. From penetration depth calculations, provided in Supporting Information Note 2, a value of 0.4 μm was obtained, which decreases the intensity of the X-ray beam in the sample by 1/e. After 3 attenuation lengths, an intensity reduction by 95% is obtained at a penetration depth of 1.5 μm, which is within the irradiated region according to the SRIM calculations (Supporting Information Note 1, 2 μm). Figures 6 and 7 provide the GI-XRD diffractograms collected on the end members and solid solutions, respectively, in a focused 2θ region between 14 and 26°.

Inspecting Figure 6, it displays clear broad features corresponding to an amorphous material. When the broad features are compared between the different data sets, a trend is apparent, such that amorphization is most pronounced in $LaPO_4$ and least in $SmPO_4$. Accordingly, it appears that amorphization occurs more readily in larger *Ln*-bearing $LnPO_4$ end-member compositions from irradiation. This trend is relatively consistent with the previous work that has examined ceramic materials,[19] where smaller element-bearing compounds tend to exhibit more radiation damage resistance, often attributed to greater difficulty in displacing heavier elements and ions.

When Figure 7 is examined for the GI-XRD diffractograms of the solid solution compositions, consistent amorphous features are also observed, similar to those of the end members seen in Figure 7. Contrastingly, a subtle trend is present where the amorphous signals appear to gain in intensity toward the $La_{0.5}Sm_{0.5}PO_4$ sample and less so for the $La_{0.5}Pr_{0.5}PO_4$ composition. The $La_{0.5}Nd_{0.5}PO_4$ sample appears to sit between these two compositions. That it displays more Bragg reflections is attributed to more crystalline micro-grains intersecting the X-ray beam during diffraction. Generally, the GI-XRD measurements indicate that radiation damage resistance worsens when there is a greater difference in the size of the *Ln* cations, namely, in $La_{0.5}Sm_{0.5}PO_4$, and improves with the more similarly sized *Ln*-bearing solid solutions, $La_{0.5}Pr_{0.5}PO_4$. In order to semiquantify the amount of amorphization that had occurred between different samples, the data were integrated using the Origin software. For this analysis, a linear baseline background correction was applied to the samples consistently as they were measured under the same parameters. An integration was then performed across the measured 2θ regions. The integrated amorphization region of the samples

https://doi.org/10.1021/acs.jpcc.6c03822
J. Phys. Chem. C 2026, 130, 11847−11858

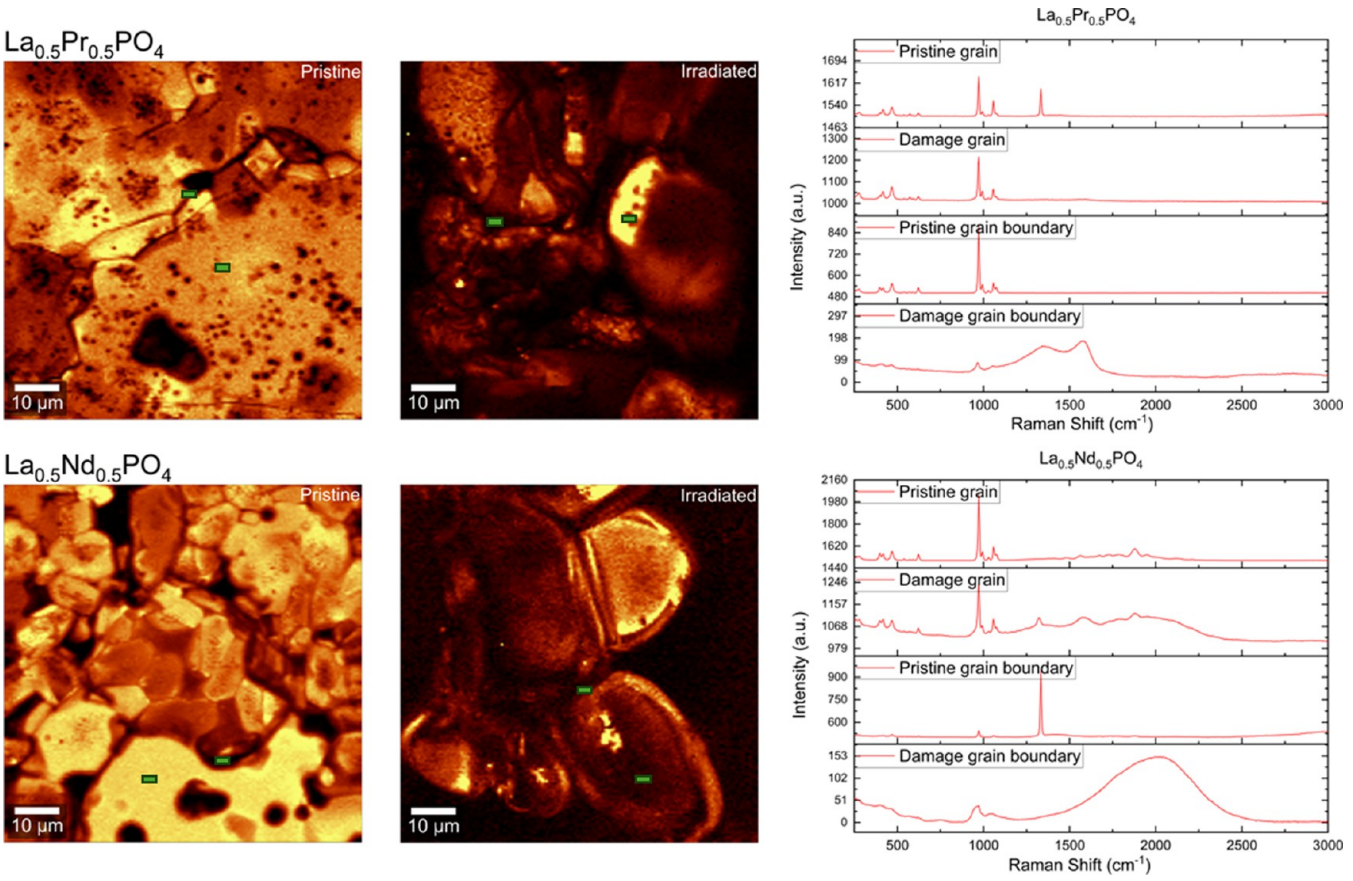

Figure 4. (Left) Raman maps of the relative intensity of the ν_1 PO_4 stretching mode for the solid solutions $La_{0.5}Pr_{0.5}PO_4$ and $La_{0.5}Nd_{0.5}PO_4$, pristine and irradiated areas. (Right) 1D Raman spectra taken by spot measurements according to the green markers given on the Raman maps.

Table 2. Determined FWHM Values Obtained via Peak Fitting of the Main ν_1 PO_4 Stretching Mode Occurring at ~970 cm^{-1} from the 1D Raman Spectra in Figures 3 and 4 with Associated Changes, Δ, to the FWHM Values Following Irradiation for the $PrPO_4$, $NdPO_4$, $La_{0.5}Pr_{0.5}PO_4$, and $La_{0.5}Nd_{0.5}PO_4$ Samples

	pristine		irradiated		Δ change	
sample	grain	grain boundary	grain	grain boundary	Δ grain	Δ grain boundary
$PrPO_4$	7.9(4)	8.1(5)	9(1)	31(4)	1(1)	23(4)
$NdPO_4$	7.8(5)	8(2)	8.4(7)	12(2)	1(8)	5(3)
$La_{0.5}Pr_{0.5}PO_4$	7.9(4)	7.9(4)	8(2)	21(2)	0(1)	13(2)
$La_{0.5}Nd_{0.5}PO_4$	8.9(4)	9.6(5)	10.1(6)	47(4)	1.2(7)	38(4)

was then normalized against that of the irradiated $LaPO_4$ sample, which presents the most amorphization from Figure 6. The results of this analysis are provided in Table 3. From Table 3, and consistent with the observations of Figures 6 and 7, the most pronounced amorphization occurs in end-member ceramics with the largest *Ln* cations (Sm → La), whereas for the solid solutions, the samples with the largest *Ln* cation size difference show the most amorphization ($La_{0.5}Pr_{.0.5}$ → $La_{0.5}Sm_{0.5}$). Moreover, the GI-XRD analysis suggests that the solid solution compositions exhibit reduced radiation damage tolerance, which is particularly pronounced when more differently sized *Ln* cations are mixed, especially the Sm and La cations.

Mechanical Properties: Vickers Indentation Microhardness and Fracture Toughness

To understand the bulk mechanical response of the investigated monazite end members and solid solutions, pristine and irradiated areas were subjected to Vickers hardness and fracture toughness testing. Figure 8a provides the microhardness as a function of average ionic radii for each composition, whereas Figure 8b provides the fracture toughness following the same dependence. Notably, for these measurements due to fragility, the $NdPO_4$ and $La_{0.5}Nd_{0.5}PO_4$ samples could not be appropriately measured.

Inspection of Figure 8a,b shows relatively similar trends between the microhardness and fracture toughness of the irradiated and pristine examined specimens. Generally, irradiation results in a decrease of both the microhardness and the fracture toughness. This indicates the materials are becoming more brittle and overall less stable from irradiation. A trend between the end members and solid solutions cannot be clearly seen from the mechanical testing regarding effects of irradiation damage. However, the use of the microindentator, which was observed to have a penetration depth of ~2−4 μm is generally deeper than the penetration depth determined from the SRIM calculations (Supporting Information Note 1). Accordingly, the results are affected by both the irradiated and

https://doi.org/10.1021/acs.jpcc.6c03822
J. Phys. Chem. C 2026, 130, 11847−11858

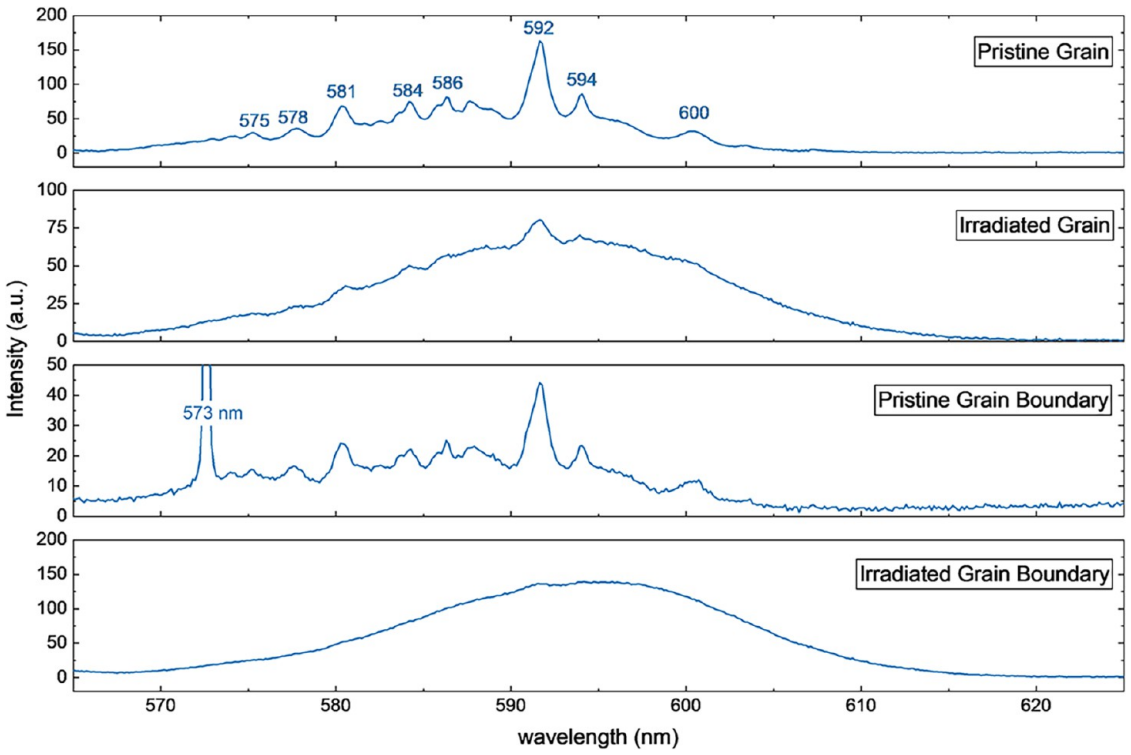

Figure 5. Nd^{3+} f−f transition region of pristine and irradiated $NdPO_4$, shown as a function of wavelength. Note: the *y*-axis scales are different for each spectrum. The wavelengths of the most prominent features are indicated in the top spectrum. These bands correspond to transitions from the nondegenerate ground state ($^4I_{9/2}$) to excited states ($^4G_{5/2}$, $^2G_{7/2}$). Following irradiation, a pronounced loss of spectral structure is observed in this region, consistent with radiation-induced disorder affecting the local order around the Nd^{3+} cation.

the pristine layers of the materials in the examined irradiated specimens; therefore, the effect of irradiated vs nonirradiated conditions could not be reliably discerned. Nevertheless, a general chemical trend can be observed in which, as the size of the *Ln* cation decreases toward Sm, the fracture toughness and mechanical toughness are observed to decrease. This result appears to be largely chemically driven, since the material densities are very similar (Table 1). Similar results have been observed previously.[20] In terms of radiation damage, there is a consistent drop in microhardness and fracture toughness compared with the pristine condition with irradiation.

DISCUSSION

The present investigation has shown that monazite ceramics $(La_{1-x}Ln_x)PO_4$ with *Ln* = Pr, Nd, and Sm, when subject to ion irradiation (14 MeV $^{197}Au^{4+}$ with 1×10^{15} ions/cm^2), exhibit reduced chemical and microstructural performance depending on whether they occur as a solid solution or as end members. A plethora of data is available for the behavior of irradiated alloys and various ceramic solid solutions,[21] but it is comparatively scarce for monazites. Generally, it is understood that the ion irradiation process creates displacement cascades that generate defects, whereby the healing response of the material is generally determined by the diffusivity of defects present, which in turn is dependent upon the specific chemistry of the ions.[22] At the same time, this process is dependent upon the mixing enthalpy of ions in solid solution, which for monazites is known to increase relative to the end-member composition.[23] In the case of Ni−Fe alloys,[24] it has been shown that radiation damage is lowered with decreasing mixing enthalpy of the solid solution, which is in turn controlled via the cation chemistry of the material's lattice constituents. The specific size difference between the constituent ions in solid solution along with associated electronic effects modulates the diffusion process and the subsequent ability of a material to respond and heal from radiation damage. Accordingly, the greater resistance observed in smaller *Ln*-bearing monazites is attributed to the difficulty in displacing these smaller and heavier cations coupled with their low mixing enthalpy. This facilitates favorable diffusivity and defect recombination. Conversely, the reduced radiation tolerance of mixed solid solutions with considerable size difference between the *Ln* cations is associated with increased mixing enthalpy, which is detrimental to radiation damage response and manifests in reduced chemical and microstructural performance, as indicated in the present investigation. However, it is stressed that further thermodynamic investigation of the irradiated materials is required to properly demonstrate this.

A further pertinent observation of this study is the role that grains and grain boundaries have in affecting the bulk irradiation damage response of materials and ceramics. Raman spectroscopy measurements and consideration of the Nd^{3+} f−f transitions identified in Figures 3−5 clearly show that a significant loss of local structural order in the PO_4 modes and also in the Nd coordination (and presumably other *Ln*'s) is most confined in the grain boundaries following irradiation. It is important to then consider the mechanisms that lead to these damage observations. Nanobeam precession electron diffraction measurements of irradiated SiC[25] have previously shown that grain boundaries act as migration sinks for ions and defects from irradiation damage, which allow a reduction in associated elastic strain. Inspection of the Raman maps (Figures 3 and 4) for the irradiated specimens shows that the grain boundary regions appear to be much larger than the

https://doi.org/10.1021/acs.jpcc.6c03822
J. Phys. Chem. C 2026, 130, 11847−11858

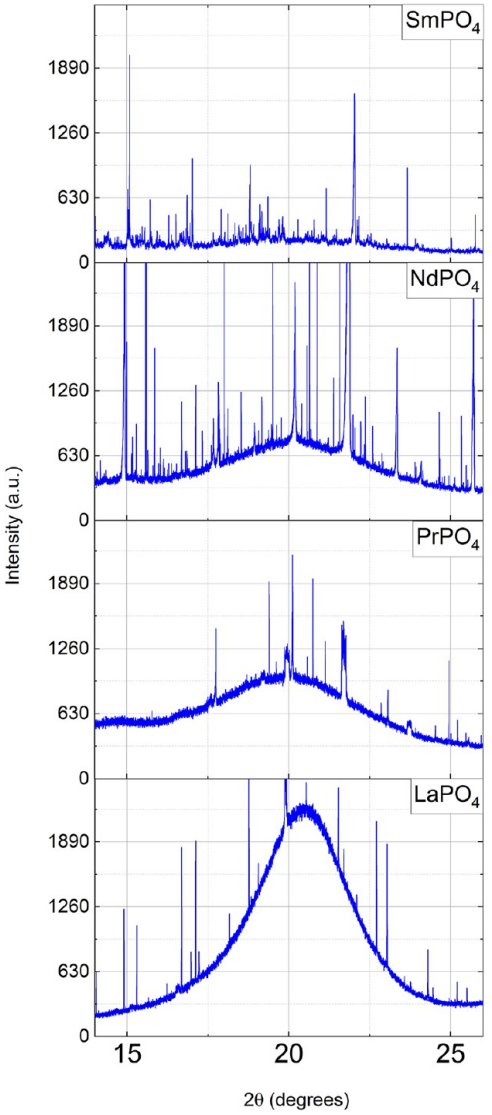

Figure 6. Synchrotron GI-XRD measurements of irradiated end-member compositions monazite ($LnPO_4$, *Ln* = La, Pr, Nd, and Sm) performed at a grazing angle of 1° with a wavelength of 1.0785 Å. Data are shown between 14 and 26° to focus on the amorphous region.

nonirradiated. This subsequently suggests that irradiation has led to their expansion and exfoliation. It would follow then that the grain boundaries are acting as sinks from retreating ions and defects during irradiation, which leads to their increased population within these regions, resulting in the associated observation of their expansion. Furthermore, as the Raman measurements show via the significant broadening of spectra and associated FWHM analysis of Table 2, the grain boundary regions exist with significant defects and distortion following irradiation, far more than that of the grains. Recent Doppler broadening measurements of He-irradiated SiC[26] showed defect clusters which pre-exist in the material act as sinks toward accumulation of irradiation-induced interstitials. Subsequently, it can be argued that pre-existing defects in the examined monazite ceramics, particularly within grain boundaries, draw defects to their positions during irradiation leading to expansion and exfoliation. The degree of exact distortion within these regions likely originates from the different chemistries of the materials as this distortion variation

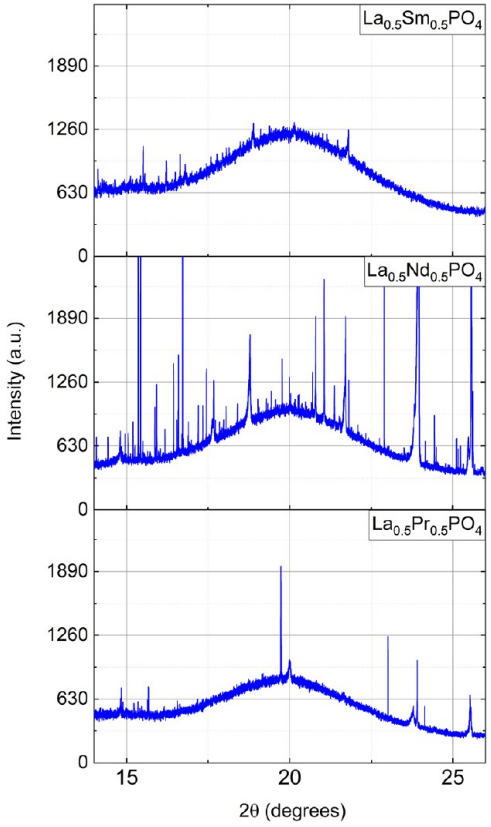

Figure 7. Synchrotron GI-XRD measurements of irradiated monazite solid solution compositions ($La_{0.5}Ln_{0.5}PO_4$, *Ln* = Pr, Nd, and Sm) performed at a grazing angle of 1° with a wavelength of 1.0785 Å. Data are shown between 14 and 26° to focus on the amorphous region. The increased amount of Bragg reflections in the $La_{0.5}Nd_{0.5}PO_4$ is attributed to smaller grain sizes intersecting the X-ray beam and diffraction.

Table 3. Determined Amorphization Amounts in Irradiated $La_{1-x}Ln_xPO_4$ (x = 0.5 and 1; *Ln* = Pr, Nd, and Sm) Samples Normalized against Irradiated $LaPO_4$, Which Presents the Greatest Amount of Amorphization from Collected Synchrotron GI-XRD Data

composition	irradiation-induced amorphization relative to $LaPO_4$
$LaPO_4$	1
$PrPO_4$	0.44
$NdPO_4$	0.36
$SmPO_4$	0.07
$La_{0.5}Pr_{0.5}PO_4$	0.37
$La_{0.5}Nd_{0.5}PO_4$	0.48
$La_{0.5}Sm_{0.5}PO_4$	0.56

is argued to be linked to the different mixing enthalpies of the end-member and solid solution samples and particularly how different ions interact during irradiation. In the context of nuclear waste form materials, this is pertinent since it influences their long-term stability, which is important for interim storage or final disposal in a repository. Moreover, it is salient to consider the radiation damage response of materials that exist as complex solid solutions rather than end members in the context of nuclear waste and spent nuclear fuel, since they readily occur in waste form materials like monazite,[27] within the fuel matrix[28] and also in cladding.[15,29]

https://doi.org/10.1021/acs.jpcc.6c03822
J. Phys. Chem. C 2026, 130, 11847−11858

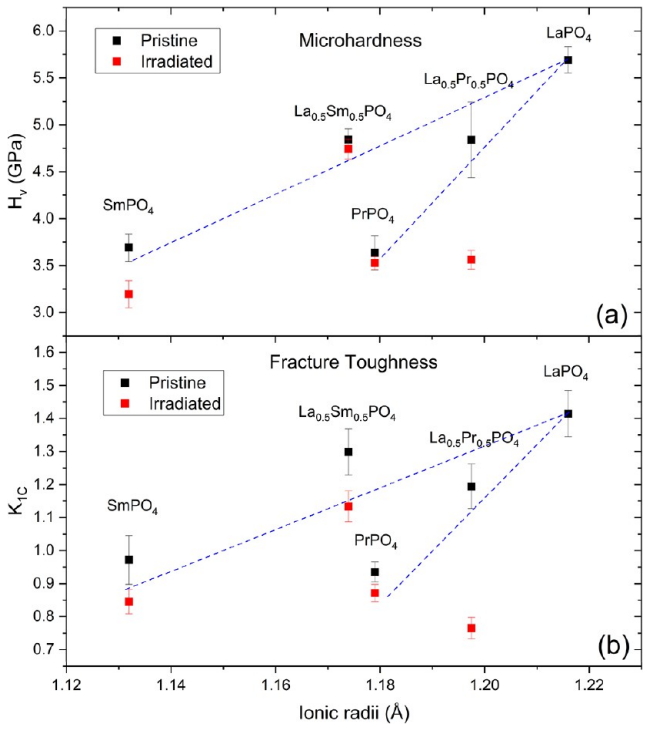

Figure 8. (a) Microhardness (H_v) of the $(La_{1-x}Ln_x)PO_4$ pellets and (b) fracture toughness with respect to the atomic radius of the average *Ln* cations present in the pellets. The pristine (preirradiation) values are given in red and the irradiated in blue. Trend lines from end members through corresponding solid solutions are given as blue dashed lines. Specific determined values are provided in Supporting Information Note 3 and Table S1.

CONCLUSIONS

To conclude, mixed monazite solid solutions $(La_{1-x}Ln)PO_4$ for *Ln* = Pr, Nd, and Sm (x = 0, 0.5, and 1) have been systematically examined with respect to their chemical, microstructural, and mechanical response to ion irradiation under conditions of 14 MeV $^{197}Au^{4+}$ ions at a fluence of 1e10^{15} ions/cm^2. SEM analysis demonstrated that reduced microstructural performance is consistently encountered for solid solution specimens where increased damage occurs as the size difference between the constituent ions increases. In contrast, end-member compositions containing the smaller and heavier *Ln* cations (e.g., $SmPO_4$) exhibit the strongest radiation damage resistance. Confocal Raman mapping measurements show that radiation damage is most pronounced in grain boundary regions of the ceramic specimens, and consideration of Raman modes indicates that radiation damage is linked to loss of regular coordination about cations via specific damage to coordinating anions (PO_4^{3-}). In the case of the Nd^{3+} bearing compositions ($NdPO_4$ and $La_{0.5}Nd_{0.5}PO_4$), resonance-enhanced electronic Raman scattering modes corresponding to f−f transitions are further identified and found to further support that damage is pronounced at grain boundaries and arises due to loss of coordination about cation centers. The degree of associated amorphization observed between end-member and solid solution samples is further found to correlate with size mismatch of *Ln* cations in solid solution behavior, as shown by GI-XRD measurements. Mechanical property testing was unable to reliably discern the effect of irradiation damage on different samples due to the indenter depth exceeding the radiation damage depth. However, it was found that the mechanical response of the ceramics does correlate with the chemistry and particularly ionic radii of *Ln* cations present; particularly, smaller *Ln*'s lead to reduced fracture toughness and microhardness. The observed reduction in radiation resistance in monazite solid solutions compared with end members is tentatively attributed to their worsened mixing enthalpy, which inhibits defect redistribution and recombination during ion irradiation and recovery and increases as the size mismatch of *Ln* cations increases. Considering the complexity of nuclear waste forms and materials arising from spent nuclear fuel, this investigation highlights the importance of studying the complexity of solid solution materials rather than more simplified end-member compounds.

ASSOCIATED CONTENT

Data Availability Statement

The data that support the findings of this study are available from the corresponding author, upon reasonable request.

Supporting Information

The Supporting Information is available free of charge at https://pubs.acs.org/doi/10.1021/acs.jpcc.6c03822.

SRIM and X-ray penetration depth calculations (PDF)

AUTHOR INFORMATION

Corresponding Author

Gabriel L. Murphy − *Institute of Fusion Energy & Nuclear Waste Management (IFN-2), Forschungszentrum Jülich GmbH, 52428 Jülich, Germany;* orcid.org/0000-0003-3239-9725; Email: g.murphy@fz-juelich.de

Authors

Mara McCleary − *Institute of Fusion Energy & Nuclear Waste Management (IFN-2), Forschungszentrum Jülich GmbH, 52428 Jülich, Germany*

Andrey Bukaemskiy − *Institute of Fusion Energy & Nuclear Waste Management (IFN-2), Forschungszentrum Jülich GmbH, 52428 Jülich, Germany*

Martina Klinkenberg − *Institute of Fusion Energy & Nuclear Waste Management (IFN-2), Forschungszentrum Jülich GmbH, 52428 Jülich, Germany*

Celina Erven − *Institute of Fusion Energy & Nuclear Waste Management (IFN-2), Forschungszentrum Jülich GmbH, 52428 Jülich, Germany*

Sara E. Gilson − *Institute of Resource Ecology, Helmholtz Zentrum Dresden-Rossendorf, 01328 Dresden, Germany;* orcid.org/0009-0007-0684-2064

Daniil Shirokiy − *Institute of Fusion Energy & Nuclear Waste Management (IFN-2), Forschungszentrum Jülich GmbH, 52428 Jülich, Germany*

Jenna Poonoosamy − *Institute of Fusion Energy & Nuclear Waste Management (IFN-2), Forschungszentrum Jülich GmbH, 52428 Jülich, Germany;* orcid.org/0000-0003-0090-1522

Felix Brandt − *Institute of Fusion Energy & Nuclear Waste Management (IFN-2), Forschungszentrum Jülich GmbH, 52428 Jülich, Germany*

Christoph Hennig − *Institute of Resource Ecology, Helmholtz Zentrum Dresden-Rossendorf, 01328 Dresden, Germany; The Rossendorf Beamline at ESRF, The European Synchrotron, 38043 Grenoble, France*

https://doi.org/10.1021/acs.jpcc.6c03822
J. Phys. Chem. C 2026, 130, 11847−11858

Andrew Fitch − *ESRF, 38043 Grenoble, France*
Shavkat Akhmadaliev − *Ion Beam Center, Helmholtz Zentrum Dresden-Rossendorf, 01328 Dresden, Germany*
Nina Huittinen − *Institute of Resource Ecology, Helmholtz Zentrum Dresden-Rossendorf, 01328 Dresden, Germany; Institute of Chemistry and Biochemistry, Freie Universität Berlin, 14195 Berlin, Germany;* orcid.org/0000-0002-9930-2329

Complete contact information is available at: https://pubs.acs.org/10.1021/acs.jpcc.6c03822

Author Contributions

The project was conceived and developed by G.L.M. Research methodology, experimental planning, and formal analysis were conducted by M.M. and G.L.M. Synthesis of materials was done by S.E.G., A.B., and C.E. Ion irradiations were performed by S.A., N.H., and S.E.G. Grazing incidence synchrotron X-ray diffraction was performed by C.H., A.F., D.S., M.M., and G.L.M. Stopping and range of ions in matter and X-ray depth penetration calculations were performed by D.S. and M.M. Electron microscopy measurements were performed by M.M., M.K., and F.B. Raman spectroscopy measurements and analysis were performed by M.M., N.H. and J.P. Manuscript writing, reviewing, and editing were performed by G.L.M. with input from all authors.

Funding

The authors are grateful for funding and support from the German Federal Ministry of Education and Research (BMBF), Project No. 02NUK060.

Notes

The authors declare no competing financial interest.

■ ACKNOWLEDGMENTS

We acknowledge the European Synchrotron Radiation Facility (ESRF) for provision of synchrotron radiation facilities under proposal number CH-7424.

■ REFERENCES

(1) (a) Ewing, R. C.; Weber, W. J.; Lian, J. Nuclear waste disposal—pyrochlore ($A_2B_2O_7$): Nuclear waste form for the immobilization of plutonium and "minor" actinides. *J. Appl. Phys.* **2004**, *95* (11), 5949−5971. (b) Weber, W. J.; Navrotsky, A.; Stefanovsky, S.; Vance, E. R.; Vernaz, E. Materials science of high-level nuclear waste immobilization. *MRS Bull.* **2009**, *34* (1), 46−53.

(2) Gilson, S. E.; Svitlyk, V.; Bukaemskiy, A. A.; Niessen, J.; Lender, T.; Murphy, G. L.; Henkes, M.; Lippold, H.; Marquardt, J.; Akhmadaliev, S.; Hennig, C.; Winkler, B.; Tonnesen, T.; Peters, L.; Fischer, C.; Huittinen, N. Microstructural investigation of Au ion-irradiated Eu-doped $LaPO_4$ ceramics and single crystals. *npj Mater. Degrad.* **2024**, *8* (1), No. 83.

(3) Lender, T.; Murphy, G.; Bazarkina, E.; Bukaemskiy, A.; Gilson, S.; Henkes, M.; Hennig, C.; Kaspor, A.; Marquardt, J.; Nießen, J.; Peters, L.; Poonoosamy, J.; Rossberg, A.; Svitlyk, V.; Kvashnina, K. O.; Huittinen, N. Investigation of radiation damage in the monazite-type solid solution $La_{1-x}Ce_xPO_4$. *Inorg. Chem.* **2024**, *63*, 17525−17535.

(4) Meldrum, A.; Boatner, L. A.; Weber, W. J.; Ewing, R. C. Radiation damage in zircon and monazite. *Geochim. Cosmochim. Acta* **1998**, *62* (14), 2509−2520.

(5) (a) Clavier, N.; Podor, R.; Dacheux, N. Crystal chemistry of the monazite structure. *J. Eur. Ceram. Soc.* **2011**, *31* (6), 941−976. (b) Dacheux, N.; Clavier, N.; Podor, R. Monazite as a promising long-term radioactive waste matrix: Benefits of high-structural flexibility and chemical durability. *Am. Mineral.* **2013**, *98* (5−6), 833−847. (c) Jardin, R.; Pavel, C. C.; Raison, P. E.; Bouëxière, D.; Santa-Cruz, H.; Konings, R. J. M.; Popa, K. The high-temperature behaviour of $PuPO_4$ monazite and some other related compounds. *J. Nucl. Mater.* **2008**, *378* (2), 167−171.

(6) Brandt, F.; Neumeier, S.; Schuppik, T.; Arinicheva, Y.; Bukaemskiy, A.; Modolo, G.; Bosbach, D. Conditioning of minor actinides in lanthanum monazite ceramics: A surrogate study with Europium. *Prog. Nucl. Energy* **2014**, *72*, 140−143.

(7) Gregg, D. J.; Farzana, R.; Dayal, P.; Holmes, R.; Triani, G. Synroc technology: Perspectives and current status. *J. Am. Ceram. Soc.* **2020**, *103* (10), 5424−5441.

(8) (a) Li, Y.; Kowalski, P. M.; Blanca-Romero, A.; Vinograd, V.; Bosbach, D. *Ab initio* calculation of excess properties of $La_{1-x}(Ln,An)_xPO_4$ solid solutions. *J. Solid State Chem.* **2014**, *220*, 137−141. (b) Thust, A.; Hirsch, A.; Haussühl, E.; Schrodt, N.; Loison, L.; Schott, P.; Peters, L.; Roth, G.; Winkler, B. Physical properties and microstructures of $La_{1-x}Pr_xPO_4$ monazite-ceramics. *Phys. Chem. Miner.* **2018**, *45* (4), 323−332. (c) Murphy, G. L.; Wang, C. H.; Zhang, Z. M.; Kowalski, P. M.; Beridze, G.; Avdeev, M.; Muransky, O.; Brand, H. E. A.; Gu, Q. F.; Kennedy, B. J. Controlling oxygen defect formation and its effect on reversible symmetry lowering and disorder-to-order phase transformations in non-stoichiometric ternary uranium oxides. *Inorg. Chem.* **2019**, *58* (9), 6143−6154.

(9) Simeone, D.; Thorogood, G. J.; Murphy, G. L.; Forestier, A.; Garcia, P.; Luneville, L. Radiation-induced micro-structures as ground states of a Swift-Hohenberg energy functional. *J. Appl. Phys.* **2019**, *125* (6), No. 065103, DOI: 10.1063/1.5072798.

(10) Babelot, C.; Bukaemskiy, A.; Neumeier, S.; Modolo, G.; Bosbach, D. Crystallization processes, compressibility, sinterability and mechanical properties of La-monazite-type ceramics. *J. Eur. Ceram. Soc.* **2017**, *37* (4), 1681−1688.

(11) Ziegler, J. F.; Ziegler, M. D.; Biersack, J. P. SRIM − The stopping and range of ions in matter (2010). *Nucl. Instrum. Methods Phys. Res., Sect. B* **2010**, *268* (11), 1818−1823.

(12) Fitch, A.; Dejoie, C.; Covacci, E.; Confalonieri, G.; Grendal, O.; Claustre, L.; Guillou, P.; Kieffer, J.; de Nolf, W.; Petitdemange, S.; Ruat, M.; Watier, Y. ID22 - the high-resolution powder-diffraction beamline at ESRF. *J. Synchrotron Radiation* **2023**, *30* (5), 1003−1012.

(13) Svitlyk, V.; dos Santos, L. B. S.; Niessen, J.; Gilson, S.; Marquardt, J.; Findeisen, S.; Richter, S.; Akhmadaliev, S.; Huittinen, N.; Hennig, C. Grazing-incidence synchrotron radiation diffraction studies on irradiated Ce-doped and pristine Y-stabilized ZrO_2 at the Rossendorf beamline. *J. Synchrotron Radiation* **2024**, *31* (2), 355−362.

(14) Ingerle, D.; Pepponi, G.; Meirer, F.; Wobrauschek, P.; Streli, C. JGIXA−A software package for the calculation and fitting of grazing incidence X-ray fluorescence and X-ray reflectivity data for the characterization of nanometer-layers and ultra-shallow-implants. *Spectrochim. Acta, Part B* **2016**, *118*, 20−28.

(15) Murphy, G. L.; Gilson, S.; Popa, K.; Prieur, D.; Schenk, S. M.; Valu, S.-O.; Ramanantoanina, H.; Prüßmann, T.; Vitova, T.; Dardenne, K.; Rothe, J.; Colle, J.-Y.; Walter, O.; Huittinen, N. Structural and chemical insights on the incorporation of americium into zircaloy-derived monoclinic zirconia. *Commun. Chem.* **2026**, *9*, No. 50, DOI: 10.1038/s42004-025-01857-9.

(16) Ruschel, K.; Nasdala, L.; Kronz, A.; Hanchar, J. M.; Többens, D. M.; Škoda, R.; Finger, F.; Möller, A. A Raman spectroscopic study on the structural disorder of monazite−(Ce). *Mineral. Petrol.* **2012**, *105* (1), 41−55.

(17) (a) Carlson, E.; Dieke, G. The state of the Nd3+ ion as derived from the absorption and fluorescence spectra of NdCl3 and their Zeeman effects. *J. Chem. Phys.* **1961**, *34* (5), 1602−1609. (b) Nawrocki, P. R.; Sørensen, T. J. Optical spectroscopy as a tool for studying the solution chemistry of neodymium (III). *Phys. Chem. Chem. Phys.* **2023**, *25* (29), 19300−19336.

(18) Lenz, C.; Thorogood, G.; Aughterson, R.; Ionescu, M.; Gregg, D. J.; Davis, J.; Lumpkin, G. R. The quantification of radiation damage in orthophosphates using confocal μ-luminescence spectroscopy of

Nd^{3+}. *Front. Chem.* **2019**, *7*, No. 13, DOI: 10.3389/fchem.2019.00013.
(19) Shirokiy, D.; Bukaemskiy, A.; Henkes, M.; Bazarkina, E. F.; Hennig, C.; Ryan, A.; Klinkenberg, M.; Güngör, M.; McCleary, M.; Marquardt, J.; Fitch, A.; Kvashnina, K. O.; Bosbach, D.; Murphy, G. L. Speciation and radiation stability of Cr and *Ln* "Grey-Phases" within Cr-doped $(Ln,U)O_2$ spent fuel model materials. *npj Mater. Degrad.* **2026**, *10*, No. 39, DOI: 10.1038/s41529-026-00752-5.
(20) Arinicheva, Y.; Bukaemskiy, A.; Neumeier, S.; Modolo, G.; Bosbach, D. Studies on thermal and mechanical properties of monazite-type ceramics for the conditioning of minor actinides. *Prog. Nucl. Energy* **2014**, *72*, 144−148.
(21) (a) Cauvin, R.; Martin, G. Solid solutions under irradiation. I. A model for radiation-induced metastability. *Phys. Rev. B* **1981**, *23* (7), No. 3332. (b) Zhang, F. X.; Ullah, M. W.; Zhao, S.; Jin, K.; Tong, Y.; Velisa, G.; Xue, H.; Bei, H.; Huang, R.; Park, C.; Weber, W. J.; Zhang, Y. Local structure of NiPd solid solution alloys and its response to ion irradiation. *J. Alloys Compd.* **2018**, *755*, 242−250. (c) Ullah, M. W.; Aidhy, D. S.; Zhang, Y.; Weber, W. J. Damage accumulation in ion-irradiated Ni-based concentrated solid-solution alloys. *Acta Mater.* **2016**, *109*, 17−22. (d) Li, Y.; Lei, Y.; Zhao, S.; Xiao, H.; Liu, H.; Wang, Y.; Luo, Y.; Zhang, J.; Wang, J.; Ewing, R. C.; Wang, C. Phase transformation and radiation resistance of *B*-site high entropy pyrochlores. *Scr. Mater.* **2023**, *229*, No. 115367.
(22) Smith, R.; Bacorisen, D.; Uberuaga, B. P.; Sickafus, K.; Ball, J.; Grimes, R. Dynamical simulations of radiation damage in magnesium aluminate spinel, $MgAl_2O_4$. *J. Phys.: Condens. Matter* **2005**, *17* (6), 875−891.
(23) Neumeier, S.; Kegler, P.; Arinicheva, Y.; Shelyug, A.; Kowalski, P. M.; Schreinemachers, C.; Navrotsky, A.; Bosbach, D. Thermochemistry of $La_{1-x}Ln_xPO_4$-monazites (*Ln* = Gd, Eu). *J. Chem. Thermodyn.* **2017**, *105*, 396−403.
(24) Jin, M.; Cao, P.; Short, M. P. Thermodynamic mixing energy and heterogeneous diffusion uncover the mechanisms of radiation damage reduction in single-phase Ni-Fe alloys. *Acta Mater.* **2018**, *147*, 16−23.
(25) Daghbouj, N.; AlMotasem, A. T.; Duchoň, J.; Li, B.; Bensalem, M.; Bahadur, F.; Munnik, F.; Ou, X.; Macková, A.; Weber, W. Nanoscale strain evolution and grain boundary-mediated defect sink behavior in irradiated SiC: Insights from N-PED and DFT. *Acta Mater.* **2025**, *303*, No. 121739.
(26) Daghbouj, N.; AlMotasem, A. T.; Li, B.; Krsjak, V.; Duchoň, J.; Ge, F.; Liedke, M. O.; Wagner, A.; Bensalem, M.; Bahadur, F. Defect landscape engineering suppresses helium damage in ceramics. *Commun. Mater.* **2026**, *7*, No. 97, DOI: 10.1038/s43246-026-01083-3.
(27) (a) Lu, K. T.; Zhang, Y.; Wei, T.; Murphy, G. L.; Bhuiyan, A.; Scales, N.; Zheng, R. LnUO4-based glass−ceramic composites as waste forms for the immobilization of lanthanide-bearing uranium wastes. *J. Am. Ceram. Soc.* **2022**, *105* (12), 7697−7709. (b) Farzana, R.; Dayal, P.; Peristyy, A.; Sutton, P.; Aly, Z.; Aughterson, R. D.; Nguyen, T. H.; Yeoh, M.; Koshy, P.; Gregg, D. J. Effect of Ti-metal addition on hot-isostatically pressed (HIPed) Synroc-C. *J. Am. Ceram. Soc.* **2023**, *106* (11), 6971−6986.
(28) (a) Murphy, G. L.; Svitlyk, V.; Henkes, M.; Shirokiy, D.; Hennig, C.; Kegler, P.; Bosbach, D.; Bukaemskiy, A. The lattice contraction of UO2 from Cr doping as determined via high resolution synchrotron X-ray powder diffraction. *J. Nucl. Mater.* **2024**, *595*, No. 155046. (b) Murphy, G. L.; Bazarkina, E.; Svitlyk, V.; Rossberg, A.; Potts, S.; Hennig, C.; Henkes, M.; Kvashnina, K. O.; Huittinen, N. Probing the Long- and Short-Range Structural Chemistry in the C-Type Bixbyite Oxides $Th_{0.40}Nd_{0.48}Ce_{0.12}O_{1.76}$, $Th_{0.47}Nd_{0.43}Ce_{0.10}O_{1.785}$, and $Th_{0.45}Nd_{0.37}Ce_{0.18}O_{1.815}$ via Synchrotron X-ray Diffraction and Absorption Spectroscopy. *ACS Omega* **2024**, *9* (25), 27397−27406.
(29) Clark, R. A.; Conroy, M. A.; Lach, T. G.; Buck, E. C.; Pellegrini, K. L.; McNamara, B. K.; Schwantes, J. M. Distribution of metallic fission-product particles in the cladding liner of spent nuclear fuel. *npj Mater. Degrad.* **2020**, *4* (1), No. 4.

https://doi.org/10.1021/acs.jpcc.6c03822
J. Phys. Chem. C 2026, 130, 11847−11858